# Analysis and Control of the Inductorless Boost Rectifier for Small Power Wind Energy Converters

Carlos Lumbreras, Juan M. Guerrero*, Daniel Fernandez, David Reigosa, Cristina Gonzalez-Moral, Fernando Briz
Email: *guerrero@uniovi.es

***Abstract*—This paper analyzes a cost-effective modification of the power topology commonly found in small wind turbine systems based on a passive rectifier and a boost converter. The boost converter inductor and the input filter capacitor often placed at the rectifier output can be replaced by the generator phase inductance. Different controller structures have been proposed for this low-cost inverter, but they have been focused in the converter itself rather than in the overall turbine control. Moreover, only steady-state behavior has been demonstrated. This paper proposes a control structure only requiring retuning of the boost current controller found in systems equipped with boost inductance; other control loops remaining unchanged. The inductorless converter dynamic performance is studied and compared with the conventional topology in terms on current and torque control capability. The system efficiency, including the losses distribution in the generator, is analyzed. Simulation and experimental results are presented to demonstrate the technical viability of this proposal.**

## I. Introduction

Nowadays, wind energy systems lead the growth in installed renewable energy power worldwide, with an installed wind power capacity increase 52.5 GW in 2017 [1]. Besides high-power wind turbines, small scale wind turbines are gaining popularity for self-energy production [2].

The energy extracted from the wind can be either stored in batteries, injected into the grid, or directly used for self-consumption feeding up local loads. Different machine types are used in wind energy systems [3]. The most common machine type used in small wind turbines is the Permanent Magnet Synchronous Generator (PMSG) since it provides a good performance within a wide speed range [3]. Several power converter topologies are used to drive the PMSG in low-power wind energy systems: back-to-back converters [4], semi-bridge switch mode rectifiers [5], [6], modifications of the back-to-back converter with a reduced number of power switches [7], [8]. Power converters proposed for the MW range, as the indirect boost matrix converter [9], [10] can also be potentially used in the upper power range of small wind turbines ($< 100$ kW). However, the most used power converter topology for low-power grid-tied systems consists of a diode rectifier and a boost converter on the generator side [11]–[14]. The lower efficiency of this topology compared with a back-to-back converter has not a meaningful impact in the annual energy production in small power systems [15].

Alternative configurations of the latter can be found in the literature. The boost coil and the input filter capacitor are displaced from the DC side to the AC side forming a three-phase LC configuration in a power factor correction application for grid-tied rectifiers [16], [17]. This topology was later applied to a PMSG-based wind energy system also placing a three-phase LC filter and a three-phase boost coil between the generator and the rectifier [18]. A similar configuration, only using the three-phase capacitor bank and three-phase boost inductor was used in [19]. The elimination of the DC capacitor after the rectifier has also been proposed to reduce the generator torque ripple [20].

A further simplification of this topology can be realized by eliminating the boost inductance, provided the generator phase inductance is sufficiently large [21]. The generator boost capability has also been exploited in other converter topologies [4], [5], [8]–[10], [22]. The inductance of long DC-link cables can be used to replace the boost inductor in large wind turbines [23], but that solution seems unfeasible in compact low-power systems. The behavior of four inductorless rectifier topologies has been investigated in [24], proposing the use of a three-phase active rectifier acting as a passive rectifier, single switch converter, semi-bridge, or active rectifier depending on the operating point.

Control of the inductorless boost converter for wind turbine applications has been investigated in [25]–[28]. The proposed control solutions in the literature focus in the converter operation at steady-state assuming either almost constant input or output power. This necessarily brings undesirable torque or grid current harmonics during transient conditions which is the usual situation in wind turbines. Furthermore, the controller dynamics and tuning are not investigated in the literature.

The efficiency of this converter compared with the one having a dedicated boost inductance has been measured in [28], showing the inductorless boost rectifier has a slightly higher efficiency. This has been explained by the boost inductor losses since the generator currents using the conventional converter have been shown to apparently contain less harmonics. However, the harmonic content and the losses distribution has not been investigated. A different conclusion is obtained in [29], where five different rectifier topologies are analytically analyzed, including the inductorless and conventional rectifiers. However, the results of this study regarding the machine losses are questionable since they are studied only comparing low frequency current harmonics. This results in zero machine losses when a three-phase active rectifier is used, and identical losses for the conventional and inductorless boost rectifier. Moreover, the comparison neglects the boost inductor losses.

This paper proposes the decoupled current control of the inductorless boost rectifier [31]. This brings an improved dynamic response from existing alternatives. Moreover, the

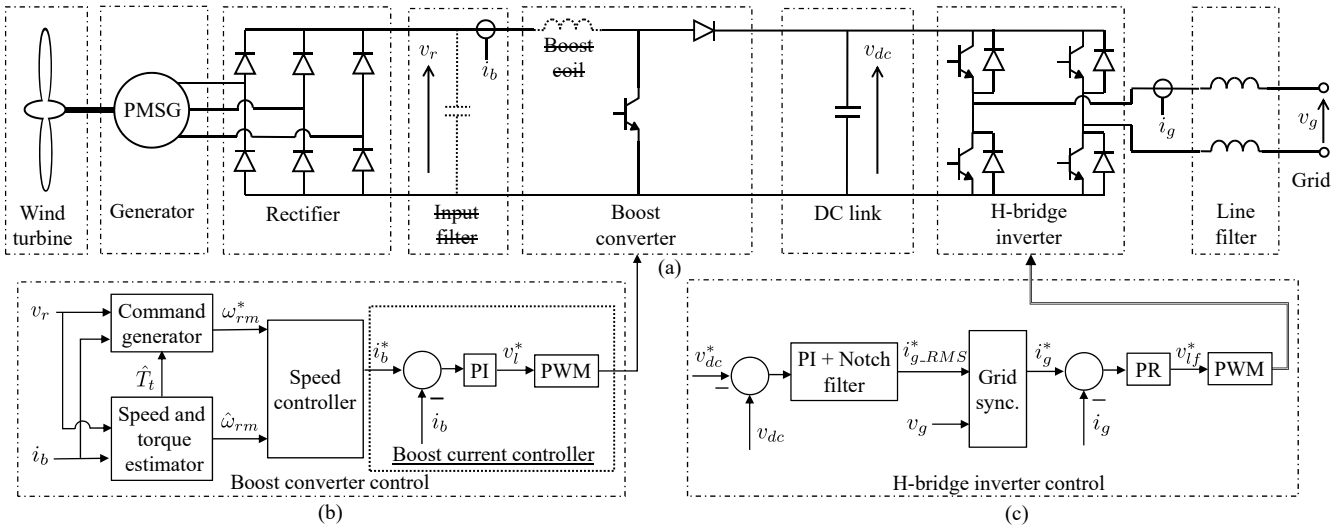


Fig. 1: Schematic representation of the wind generation system [30]. The input filter and the boost coil are removed in the inductorless topology. (a) Turbine, generator and power converters. (b) Boost converter control system. (c) H-bridge inverter control system.

TABLE I Coil design conditions

| | |
|---|---|
| Core material | Iron powder |
| Relative permeability $\mu_r$ | 60 |
| Maximum flux density, $B_{sat}$ | 1.6 T |
| Switching frequency | 20 kHz |
| Rated current | 6 A |
| Peak current | 10 A |

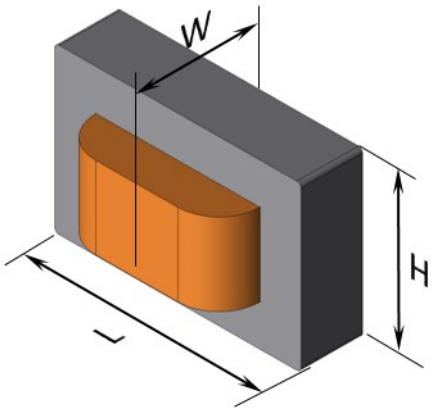


Fig. 2: Coil dimensions

proposed controller does not require control hardware changes from the conventional converter allowing direct retrofitting of existing systems. The converter model for tuning the controller is provided and the dynamic response analyzed. The inductorless converter is compared with the conventional one in terms of current and torque control capability, the latter being ignored by previous studies. Moreover, the impact of removing the boost inductance in the generator losses is studied in detail, which has not been previously addressed. This is key to validate the use of this converter with permanent magnet generators since the magnets can be easily demagnetized under high temperature.

## II. System description

### A. Power converter

The most common power converter topology for grid-tied low power wind turbines is based on a passive rectifier, a boost converter, and an H-bridge inverter, as shown in Fig. 1(a). The wind turbine is coupled to a permanent magnet synchronous generator in direct-drive configuration. The machine terminals are connected to a diode rectifier. A boost converter increases the rectified back-emf voltage to a level higher than the grid voltage peak magnitude. This allows to inject current into the grid using a single-phase full bridge inverter and a line filter.

The boost converter is required when the generator voltage rating is lower than the grid voltage, or more precisely, the DC-link voltage. The boost inductance withstands the voltage difference between the DC-link voltage and the voltage at the generator terminals. In systems using generators with a voltage rating similar or higher than the grid voltage, the boost converter is also required to enable the injection of current into the grid at low rotor speed. However, in the latter the boost inductance can be removed since there is no need of protect the motor against a high voltage at its terminals. In this case the voltage boost function can be achieved by the generator stator phase inductances. The stator inductance in low power PMSG is generally large enough to provide the boost capacity required for the generator voltage. Therefore, this paper further investigates the elimination of the boost coil found in these systems, as seen with a dotted line in Fig. 1(a). This will automatically bring a size and cost reduction. This modification can be easily introduced even in existing low-power turbine converter designs.

To give a better idea on the size and cost reduction that this modification can bring to the system, a design study has been conducted. The boost coil design conditions shown in table I have been used as base figures for our system, for the design of an E-core type coil, as seen in Fig. 2. The final size will depend on the goal inductance that will be selected

TABLE II Coil dimensions and cost

| Target L (mH) | L (mH) | Heigth (mm) | Length (mm) | Width (mm) | Weight (g) | Core type | Turns | Wire ⌀ (mm) | Core cost (€) | Copper cost (€) | Total cost (€) |
|---|---|---|---|---|---|---|---|---|---|---|---|
| 1 | 1.008 | 42.2 | 42.8 | 59 | 554 | 4321C | 65 | 3x1.6 | 8 | 1.7 | 9.7 |
| 2.5 | 2.513 | 55,2 | 54.9 | 82.4 | 1292 | 5528A | 81 | 3x1.64 | 18 | 2.65 | 20.65 |
| 5 | 5.017 | 65 | 65.1 | 105.2 | 2291 | 6533A | 98 | 3x1.75 | 30 | 4.1 | 34.1 |
| 7.5 | 7.549 | 65 | 65.1 | 132.2 | 3079 | 6533A | 108 | 3x1.68 | 40 | 5.7 | 45.7 |
| 10 | 10.063 | 65 | 65.1 | 159.2 | 3867 | 6533A | 114 | 3x1.64 | 50 | 7.3 | 57.3 |

according to the allowable ripple in the boost current. Table II summarizes the dimensions, weight and coil for inductance values ranging from 1 mH to 10 mH. The cost of the core and copper have been calculated for reference using retail prices. Manufacturing cost are not included.

The boost converter input filter capacitor commonly placed at the rectifier output, also seen with a dotted line in Fig. 1(a), must be also removed to avoid short-circuit when the boost converter switch is on. This will bring additional benefits in term of size, cost and reliability.

The variables often sensed to operate the wind turbine in this type of systems, seen in Fig. 1(a), are the rectifier voltage, $v_r$, the boost current, $i_b$, the DC-link voltage, $v_{dc}$, and the grid current and voltage, $i_g$ and $v_g$ respectively. The proposed converter controller uses the same set of variables. However, the rectifier voltage will be now a switching signal since the rectifier output is directly connected to the boost converter switch. If an anti-aliasing filter was being used to interface the voltage sensor output to the analog-to-digital (AD) converter, no further modification is needed. An anti-aliasing filter with a cut-off frequency of 3.5 kHz is used in this study. If analog filters were not used in the original system, a simple RC filter network can be placed between the sensor output and the AD converter [31].

### *B. Control systems*

The modification of the boost converter does not necessarily introduce changes in the control strategy followed when a conventional converter is used, and virtually any control alternative for conventional converters found in the literature could be potentially applied. Only the boost current controller will require further attention as will be in-depth explained in section III.

The control strategy proposed in [30] has been used in this study, and it will be briefly described next. However, the method has been also satisfactory tested [31] with the control method proposed in [14].

The control of the wind energy system is structured in two independent control subsystems as it is seen in Fig. 1(b)-(c).

The boost converter controller seen in Fig. 1(b) ultimately controls the power extracted from the wind. The inputs for this controller are the rectifier voltage and the boost current. A rotor speed command, $\omega^*_{rm}$, is generated from these two variables to follow a maximum power point tracking (MPPT) trajectory. At the same time a rotor speed estimate, $\hat{\omega}_{rm}$, is obtained from the same variables. The turbine torque, $T_t$, is also estimated for high wind speed protection, being $\hat{T}_t$ in Fig. 1(b) the estimated turbine torque. A speed controller produces a boost current command using the previous signals as inputs, provided the boost current is proportional to the generator torque. The implementation details can be found in [30]. The boost current command is then the input of a current controller, highlighted in Fig. 1(b). As it was earlier mentioned, only this block will require some modification with the inductorless converter, making this solution distinct to those previously reported [25]–[28].

The boost current needed to brake the wind turbine will be injected into the DC link seen in Fig. 1(a) increasing the DC-link voltage. The H-bridge inverter controller seen in Fig. 1(c) regulates the DC-link voltage using a cascaded control structure. The inner loop controls the current injected into the grid using a proportional-resonant (PR) controller, while the outer loop controls the DC-link voltage using a PI controller improved with a notch filter. The DC output of this controller, $i^*_{g\_\mathrm{RMS}}$, is converted into an AC reference for the PR current controller, $i^*_g$, using a grid synchronization block (i.e. phase-lock loop). The H-bridge controller does not require any modification by using the inductorless converter. It must be remarked that the converter modifications only affect to the boost converter. Therefore, this solution can be also applied to step-up battery systems.

## III. Boost current controller design

The boost inductance and the input filter removal in the boost converter will introduce some changes in the boost current controller, seen in Fig. 1(b). For the sake of clarity, a recall on the design of the current controller using the conventional topology will be firstly made.

### *A. Conventional converter*

Fig. 3(a) shows the conventional boost converter topology used in low power wind turbines. The measured variables are the rectifier voltage, $v_r$, the DC-link voltage, $v_{dc}$, and the boost current, $i_b$. The average voltage across the inductance, $v_l$, in a pulse width modulation (PWM) period can be calculated as a function of the PWM duty cycle, $d$, assuming continuous conduction mode (1).

$$v_l = v_r + v_{dc} \times (d-1);\ 0 \leq d \leq 1 \tag{1}$$

Therefore, a simple transfer function model considering $v_l$ as input and $i_b$ as output can be considered (2)

$$G(s) = \frac{i_b(s)}{v_l(s)} = \frac{1}{L_b s + r_b} \tag{2}$$

where $L_b$ and $r_b$ are the inductance and the resistance of the boost coil respectively, and $s$ is the Laplace variable.

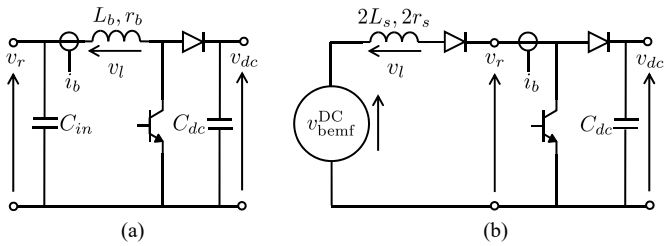


Fig. 3: Schematic representation of the boost converter. (a) Conventional. (b) Inductorless.

TABLE III
GENERATOR PARAMETERS

| | | |
|---|---|---|
| Rated power | $P_g$ | 1.7 kW |
| Rated speed | $\omega_{rm}$ | 500 r/min |
| Rated current | $i_r$ | 3.7 A |
| Stator resistance | $r_s$ | 6.03 Ω |
| Inductance | $L_d = L_q$ | 63 mH |
| Back-emf constant | $k_e$ | 1.06 $V_{peak}$/r/min |
| Pole number | $p$ | 12 |
| Inertia constant | $J_g$ | .00581 kg $m^2$ |

A proportional-integral (PI) controller with gains tuned using zero-pole cancellation provides the desired closed-loop bandwidth (3). The controller output being the voltage across the inductance command, $v_l^*$, as seen in Fig. 1(b), which is converted into a duty cycle value by finding $d$ in (1), since $v_r$ and $v_{dc}$ are known (i.e. measured) magnitudes.

$$PI(s) = k_p + \frac{k_i}{s};\ k_p = 2\pi \text{bw} L_b,\ k_i = 2\pi \text{bw} r_b \qquad (3)$$

where $k_p$ and $k_i$ are the proportional and integral gains respectively, and bw is the desired closed-loop bandwidth in Hz.

### *B. Inductorless converter*

The schematic representation of the inductorless converter can be seen in Fig 3(b). In a three-phase passive rectifier, the two AC phases having the highest and the lowest voltage are connected to the DC output. Therefore, a DC equivalent model of the AC machine can be considered as seen in Fig 3(b), where a DC-equivalent back-emf voltage, $v_{bemf}^{\text{DC}}$, can be given by (4) [32], and the two conducting phases can be seen as a single coil with an inductance and resistance being the sum of both phases.

$$v_{\text{bemf}}^{\text{DC}} = \max(v_{as}, v_{bs}, v_{cs}) - \min(v_{as}, v_{bs}, v_{cs}) = \\ = \frac{3\sqrt{3}}{\pi} V_{\text{bemf}} \left(1 - \sum_{n=1}^{\infty} \frac{2}{(6n)^2 - 1} \cos(6n\omega_r t)\right) \qquad (4)$$

where $v_{as}$,$v_{bs}$ and $v_{bs}$ are the generator phase currents, $V_{\text{bemf}}$ is the peak amplitude of the generator back-emf voltage, $\omega_r$ is the generator electrical speed, and $n$ is the harmonic number.

The transfer function given by (2) still holds for the inductorless converter by replacing the inductance and resistance values by $2L_s$ and $2r_s$ respectively, and neglecting the diode forward voltage. Therefore, the PI controller gain tuning follows the same procedure shown by (3) with the new inductance and resistance values.

The average voltage across the generator equivalent boost inductance, seen in Fig 3(b), in a PWM period is given by (5), assuming continuous conduction mode.

$$v_l = v_{\text{bemf}}^{\text{DC}} + v_{dc} \times (d-1);\ 0 \le d \le 1 \qquad (5)$$

Since $v_{\text{bemf}}^{\text{DC}}$ is not measured, an approximation is required to calculate the duty value once the voltage across the coil command, $v_l^*$, is calculated by the PI controller. Three options have been tested: 1) The measured rectifier voltage, $v_{r\_\text{DSC}}$; 2) The measured rectifier voltage, $v_{r\_\text{DSC}}$, after low-pass filtering: $v_{r\_\text{LPF}}$; 3) An estimate of the average (i.e. DC) value of $v_{\text{bemf}}^{\text{DC}}$ obtained from $v_{r\_\text{DSC}}$ and the measured boost current $i_{b\_\text{DSC}}$, after low-pass filtering. The first option gives poor results since the signal ripple lags the ripple content of $v_{r\_\text{DSC}}$. The second and third options give identical results, since the low bandwidth estimation of the third option is easily achieved by the current controller if the low-pass filtered rectifier voltage is used. Therefore, for simplicity, the voltage across the generator-equivalent boost inductor will be calculated as (6).

$$\hat{v}_l = v_{r\_\text{LPF}} + v_{dc} \times (d-1);\ 0 \le d \le 1 \qquad (6)$$

where $\hat{v}_l$ is the estimated voltage across the equivalent boost coil.

This approximation will introduce some distortion in the voltage command due to the actual ripple content of the back-emf voltage. The next section analyzes its effect in the boost current obtained.

## IV. Boost current controller performance

The current controller has been first tested using detailed simulations to analyze not only the boost current control, but also the corresponding torque produced. It must be remarked that the main goal of controlling the boost current is to indirectly control the generator torque.

Matlab/Simulink software package has been used for the simulations. Discrete-time controllers have been obtained using Tustin approximation, and they have been implemented in C language. Therefore, the same control code runs in the simulation as in the actual digital signal controller (DSC). A PWM and sampling frequency of 20 kHz is used for the boost converter control. AD and PWM quantization and 3.5 kHz antialiasing filters are introduced in the simulation model to match the experimental setup conditions. A PMSG model with the same parameters as the actual generator used in the experimental study has been used. The generator parameters can be found in Table III. The machine simulation model does not include cogging torque.

Fig. 4 demonstrates the current controller capability. A boost current current command is increased from 0 to 6 A in 1 A steps every half second when the generator rotor speed is fixed to 400 r/min. The boost current controller bandwidth is tuned to 400 Hz. Fig. 4(a) shows the actual current, $i_b$, while Fig. 4(b) shows the current measured by

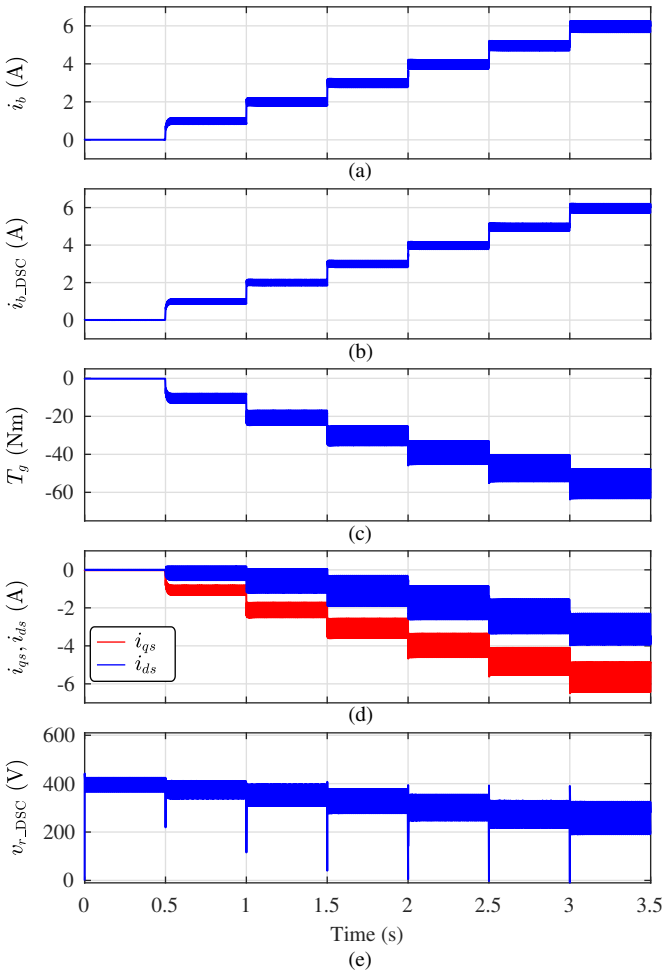


Fig. 4: Simulation. Inductorless boost converter performance. 1 A boost current steps at fixed 400 r/min rotor speed. Current loop bandwidth: 400 Hz. (a) Boost current, $i_b$. (b) Measured boost current, $i_{b\_DSC}$. (c) Generator torque, $T_g$. (d) $q-$ and $d-$axes stator current in synchronous reference frame. (e) Measured rectifier voltage after the antialiasing filter, $v_{r\_DSC}$.

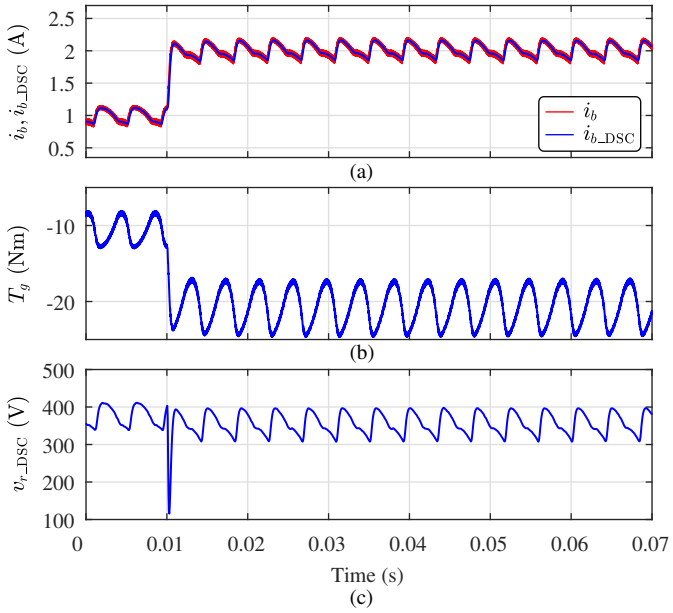


Fig. 5: Simulation. Inductorless boost converter performance detail. 1 to 2 A boost current step at fixed 400 r/min rotor speed. Current loop bandwidth: 400 Hz. (a) Actual and measured boost current, $i_b$ and $i_{b\_DSC}$ respectively. (b) Generator torque, $T_g$. (c) Measured rectifier voltage, $v_{r\_DSC}$.

TABLE IV
BOOST CONVERTER PARAMETERS

| | | |
|---|---|---|
| Input filter capacitance | $C_{in}$ | 235 µF |
| Boost coil inductance | $L_b$ | 5 mH |
| Boost coil resistance | $r_b$ | 0.6 Ω |
| DC-link capacitance | $C_{dc}$ | 235 µF |

the DSC (i.e. filtered, quantized and sampled), $i_{b\_DSC}$. The line thickness is due to the AC ripple present in the signals. Both signals are similar and show a moderate ripple content at the harmonic frequencies present in $v_{\text{bemf}}^{\text{DC}}$. This is due to the voltage command approximation (6). This is more clearly seen in the magnified view shown in Fig. 5(a). The switching harmonics are negligible due to the large equivalent boost inductance (twice the stator inductance). Moreover, there is not a significant increase of the current ripple with increasing load, as can be seen in Fig. 4(a)-(b). Fig. 4(c) shows the corresponding generator torque. It also shows AC harmonic content corresponding to the back-emf harmonic frequencies. A detailed view can be seen in Fig. 5(b). However, in this case the torque ripple magnitude is load dependent, as can be seen in Fig. 4(c). However, this torque ripple is not expected to be an issue for the turbine speed control due to the large turbine inertia. The reason for this torque ripple increase is found in the $q-$ and $d-$axes components of the stator current that show an increasing ripple magnitude with the load level [see Fig. 4(d)]. The measured and filtered rectifier voltage, $v_{r\_DSC}$ can be seen in Fig. 4(e). When the boost current is zero and the power switch is open, the rectifier voltage equals the back-emf voltage. The signal used for the turbine control is $v_{r\_DSC}$ which detailed view can be found in Fig. 5(c).

The current controller shows a good dynamic response, as seen in Fig. 5(a), but even more important, a similar dynamic response can be seen for the generator torque in Fig. 5(b).

This section has demonstrated the inductorless converter capability with the proposed control structure for controlling the boost current and the generator torque. Next section analyzes the advantages and limitations when compared with the conventional topology.

## V. Comparison with the Conventional Boost Converter

This section discusses the differences between the inductorless converter and the conventional converter in the boost current control, resulting generator torque, harmonic current content in the electrical machine, and efficiency. A boost converter with the parameters seen in Table IV is used for comparison.

### A. Boost current control and generator torque

The same simulation conditions explained for Figs. 4 and 5 have been reproduced using the conventional converter in Figs. 6 and 7.

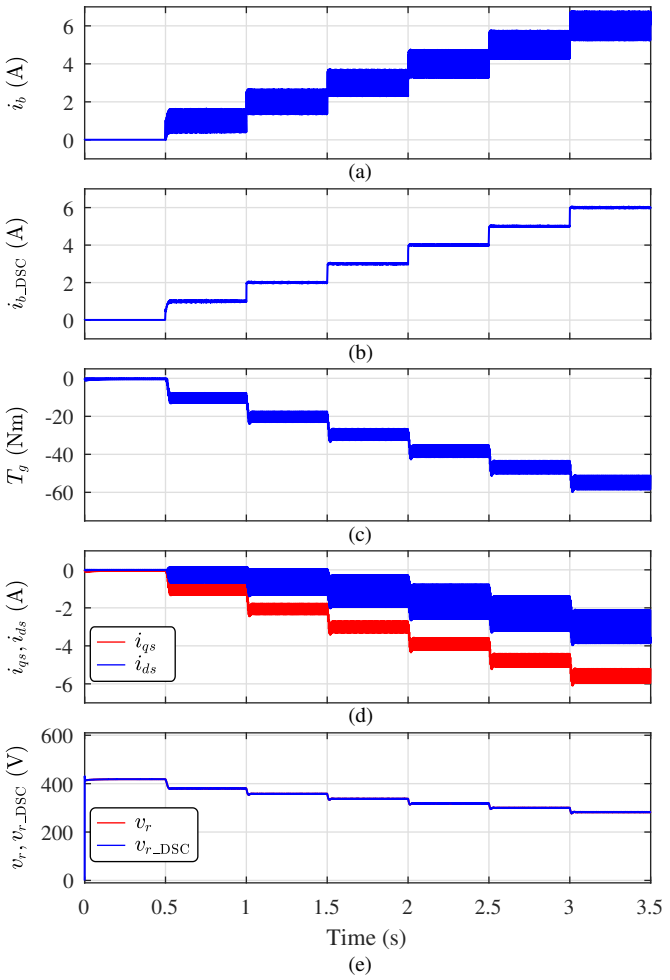


Fig. 6: Simulation. Conventional boost converter performance. 1 A boost current steps at fixed 400 r/min rotor speed. Current loop bandwidth: 400 Hz. (a) Boost current, $i_b$. (b) Measured boost current, $i_{b\_\mathrm{DSC}}$. (c) Generator torque, $T_g$. (d) $q-$ and $d-$axes stator current in synchronous reference frame. (e) Actual and measured rectifier voltage, $v_r$ and $v_{r\_\mathrm{DSC}}$ respectively.

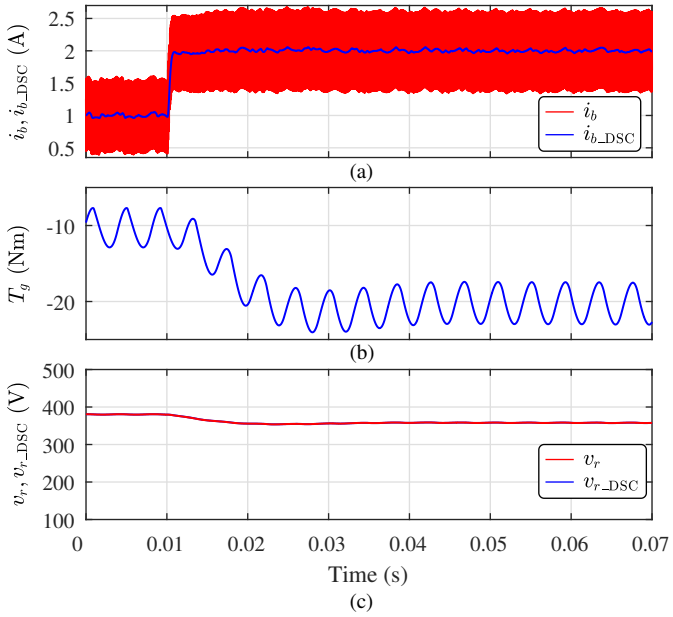


Fig. 7: Simulation. Conventional boost converter performance detail. 1 to 2 A boost current step at fixed 400 r/min rotor speed. Current loop bandwidth: 400 Hz. (a) Actual and measured boost current, $i_b$ and $i_{b\_\mathrm{DSC}}$ respectively. (b) Generator torque, $T_g$. (c) Measured rectifier voltage, $v_{r\_\mathrm{DSC}}$.

Fig. 6(a)-(b) shows the actual current, $i_b$, and the sampled current, $i_{b\_\mathrm{DSC}}$. In this case, the actual current has a significant amount of ripple, while the sampled current is a clean signal. The reason is now the ripple is due to high frequency switching harmonics, as seen in Fig. 7, which are not seen by the sampled signal. Since the voltage command provided by the PI controller is correctly calculated by (2), there are no back-emf dependent harmonics in the controlled signal, $i_{b\_\mathrm{DSC}}$. The corresponding generator torque can be seen in 6(c). The average value of the torque is similar for the same boost current level. Despite the average current, $i_{b\_\mathrm{DSC}}$, does not contain back-emf dependent harmonics, the generator torque does, as can be better seen in Fig. 6(b). This is explained by the fact the $q-$ and $d-$axes stator current components contain that harmonic content. However, when compared with the inductorless converter the torque ripple is not load dependent, showing a smaller magnitude at medium to large load. It can be also seen that switching harmonics are not present neither in the generator currents nor the torque. This is due to the effect of the input filter capacitor. The rectifier voltage is shown in Fig. 6(e) and Fig. 7(c) for reference.

An important advantage of the inductorless converter can be seen by comparison of Figs. 5 and 7. While the current control dynamics are similar in both cases [see Figs. 5(a) and 7(a)], the generator torque response is slower for the conventional converter, as seen in Figs. 5(b) and 7(b). This can be explained by the fact the boost current in the conventional case is decoupled from the generator current to some extent by the input filter capacitor.

### *B. Generator current harmonics and power losses*

One concern with the inductorless inverter is the distribution of the power losses once the boost coil is removed, as well as the total system efficiency. It has been shown in the previous subsection that the same average torque is produced for the same boost current level. Therefore, comparisons between both alternatives will be made in terms of the boost current level.

Fig. 8(a) shows two periods of the generator phase-$a$ current when the boost current command is 2 A and the rotor speed is fixed to 400 r/min (i.e. 40 electrical Hz), for both the inductorless and the conventional converter. They show a similar magnitude and shape distortion. The Fast Fourier Transform (FFT) is applied to analyze the frequency spectrum of both signals. Fig. 8(b) show the per unit (p.u.) FFT magnitude relative to the fundamental frequency component magnitude at 40 Hz. The frequency range shown in Fig. 8(b) has been limited to those frequency components having a magnitude larger or equal to 0.01 p.u. The total harmonic distortion (THD) is calculated for harmonics up to 1 kHz. Both converters create a similar low-frequency harmonic distribution in the generator currents for this boost current level. This agrees with the similar torque ripple level seen in Figs. 5(c) and 6(c) for

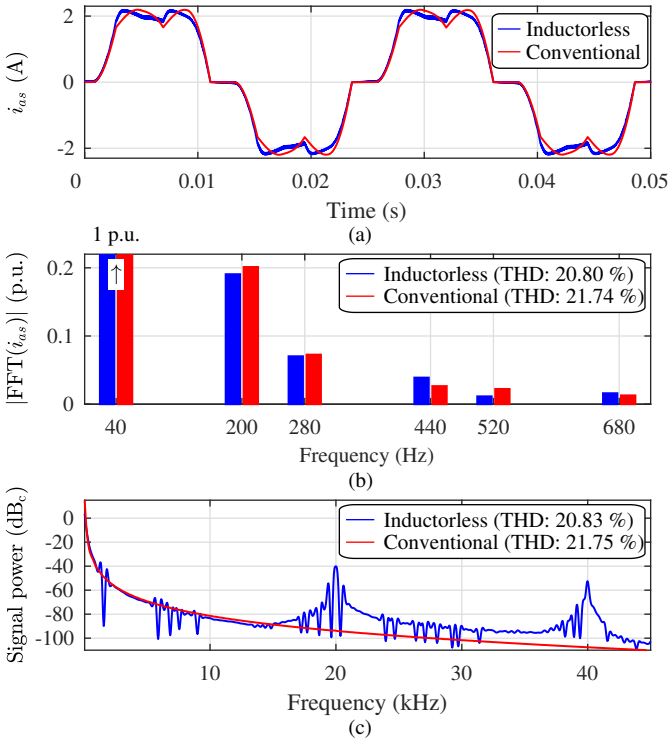


Fig. 8: Simulation. Generator phase-a current with boost current $i_b = 2$ A, rotor speed $\omega_{rm} = 400$ r/min and DC-link voltage $v_{dc} = 575$ V, for the inductorless and conventional boost converters. (a) Phase-$a$ current. (b) Frequency spectrum of phase-$a$ current showing components higher than .01 p.u. THD calculated for harmonics up to 1 kHZ. (c) Power spectrum of phase-$a$ current. THD for harmonics up to 45 kHZ.

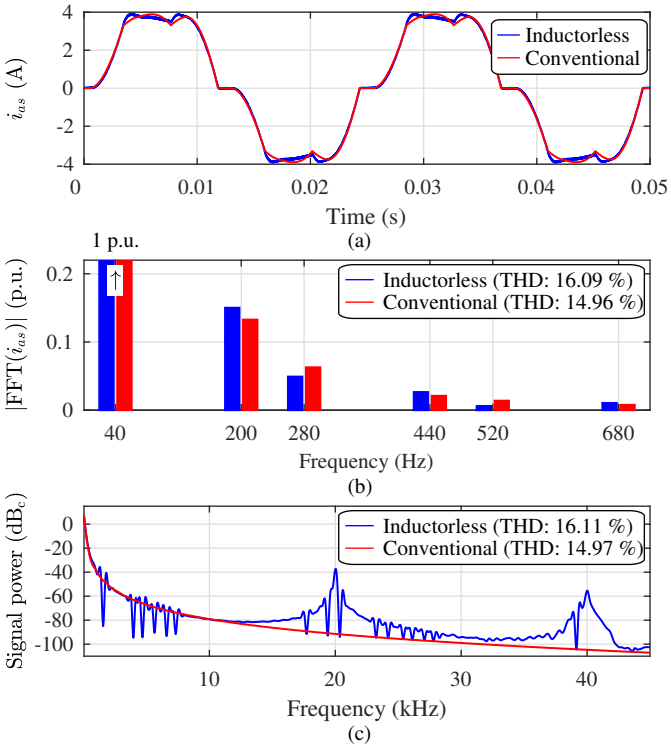


Fig. 9: Simulation. Generator phase-a current with boost current $i_b = 3.7$ A (rated), rotor speed $\omega_{rm} = 400$ r/min and DC-link voltage $v_{dc} = 575$ V, for the inductorless and conventional boost converters. (a) Phase-$a$ current. (b) Frequency spectrum of phase-$a$ current showing components higher than .01 p.u. THD calculated for harmonics up to 1 kHZ. (c) Power spectrum of phase-$a$ current. THD for harmonics up to 45 kHZ.

this current level. To evaluate the effect of switching harmonics the signal power spectrum is shown in 8(c), where the THD is calculated for frequencies up to 45 kHz. Above this frequency there is no meaningful change in THD. A low impact in the inductorless converter torque production can be expected from these harmonics, and nonexistent in the conventional converter case. Nevertheless, they can contribute to increased iron losses.

When the boost current level increases, the low-frequency harmonic content relatively decreases compared with the fundamental waveform, as can be seen in Fig. 9. It shows the same signals as Fig. 8 with a boost current of 3.7 A (rated). However, the inductorless converter exhibits a smaller reduction. This is in agreement with the larger torque ripple seen as the boost current level increases. Nevertheless, there is not a dramatic difference between both converters. The high frequency harmonics remain at a similar relative level as can be seen in Fig. 9(c).

Finite Element Analysis (FEA) using the ANSYS/Maxwell software package has been conducted to precisely determine both the copper and iron losses using both converters. A FEA model mimicking the actual PMSG used in the experimental setup has been developed as seen in Fig. 10. The main parameters can be found in Table III. The boost coil used in the conventional converter has been also modeled. Its parameters can be found in Table IV.

Fig. 11 shows the losses' distribution for both converters when different boost current levels are imposed, and the rotor

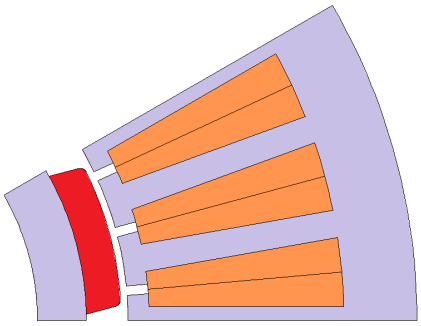

Fig. 10: Cross-section of the generator model developed for finite element analysis

speed is fixed to 400 r/min. It only includes the generator and the boost coil losses in the conventional converter case; the losses in the input filter capacitor being neglected. Fig. 11(a) shows the copper losses. The generator losses are similar in both cases, and the coil losses are small. However, the inductorless converter shows less total losses. Fig. 11(b) shows the hysteresis losses. Again, the generator losses are similar in both cases but due to the coil losses the inductorless converter is a better option. Fig. 11(c) shows the Eddy current losses. In this case the generator losses are slightly higher in case of the inductorless inverter. This is due to the switching harmonics present in the phase currents, not seen in the conventional case. Nevertheless, the losses in the coil are much higher than this difference due to the high switching ripple in the boost current.

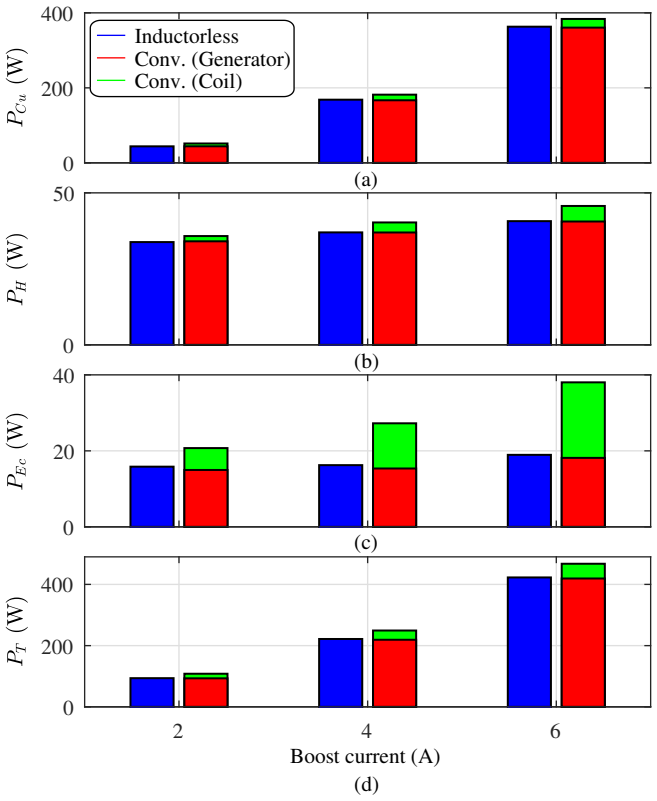


Fig. 11: FEA. Generator power loss distribution for different boost current levels and fixed rotor speed, $\omega_{rm} = 400$ r/min, using the inductorless and the conventional converter. Power losses in the boost coil are shown for the conventional converter. (a) Copper losses. (b) Hysteresis losses. (c) Eddy current losses. (d) Total losses.

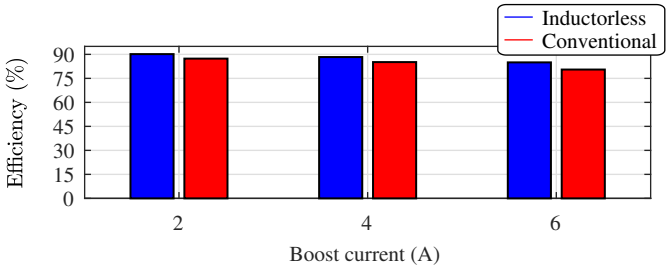


Fig. 12: FEA. Generator efficiency for different boost current levels and fixed rotor speed, $\omega_{rm} = 400$ r/min, using the inductorless and the conventional converter. The conventional converter case includes the boost coil losses.

Fig. 11(d) shows the total losses. The generator losses in the inductorless case are slightly higher at medium to high load. However, the coil contribution to the total losses makes the inductorless converter a more efficient solution. The resulting efficiency for the same cases is shown in Fig. 12. It has been calculated using (7).

$$\text{Efficiency} = \frac{P_{\text{mech}} - P_T}{P_{\text{mech}}} \tag{7}$$

where $P_{\text{mech}}$ is the mechanical power calculated using the average torque and the rotor speed, and $P_T$ are the total losses seen in Fig. 11(d).

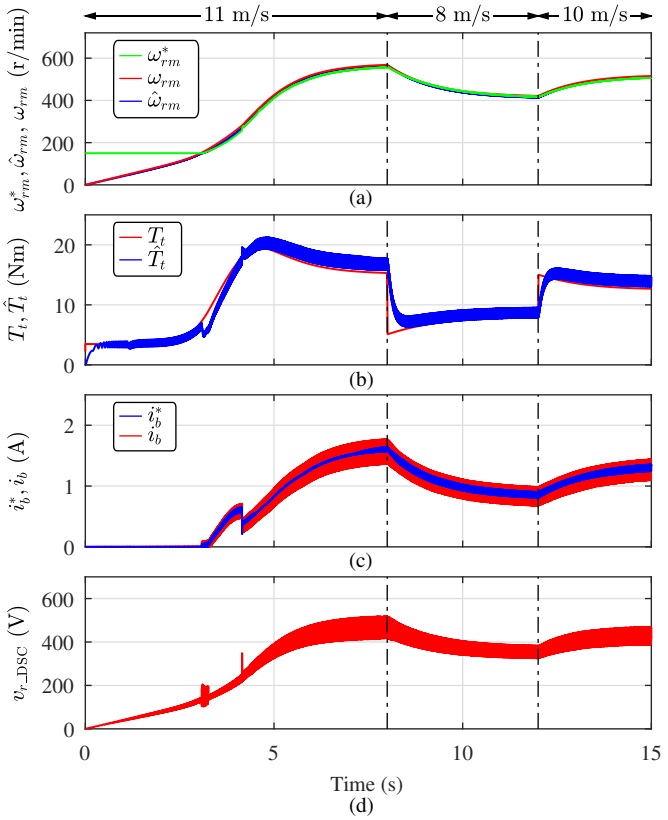


Fig. 13: Simulation. Wind turbine control performance under variable wind conditions (11, 8, and 10 m/s indicated on top of figure). (a) Rotor speed command, $\omega^*_{rm}$, and actual and estimated rotor speed, $\omega_{rm}$ and $\hat{\omega}_{rm}$ respectively. (b) Actual and estimated turbine torque, $T_t$ and $\hat{T}_t$ respectively. (c) Boost current command and actual current, $i^*_b$ and $i_b$ respectively. (d) Measured rectifier voltage, $v_{r\_\text{DSC}}$.

TABLE V
TURBINE PARAMETERS

| | | |
|---|---|---|
| Rated power output | $P_t$ | 1.2 kW |
| Rated wind speed | $v_w$ | 12 m/s |
| Rated rotor speed | $\omega_{rm}$ | 600 r/min |
| Turbine radius | $R$ | 0.875 m |
| Mechanical inertia | $J_t$ | 0.74 kg · m$^2$ |
| Optimal TSR | $\lambda_{max}$ | 4.6 |
| Optimal power coefficient | $c_{p\_max}$ | 0.47 |

## VI. Wind Turbine Control

The inductorless converter has been tested to control a wind turbine using the control strategy described in section II-B. A turbine model with the parameters shown in Table V has been used in this study.

Fig. 13 shows a case where the turbine is operating in the maximum power point tracking (MPPT) region. The turbine starts with a wind speed of 11 m/s, that later changes to 8 m/s and finally to 10 m/s as indicated on top of Fig. 13. The wind turbine must follow the rotor speed command, $\omega^*_{rm}$, seen in Fig. 13(a), which is calculated by the command generator block seen in Fig. 1(b) to follow the MPPT trajectory. The speed command tracking is successfully achieved by the inductorless system as can be seen in Fig. 13(a). The analyzed torque ripple does not create speed oscillations due to the large

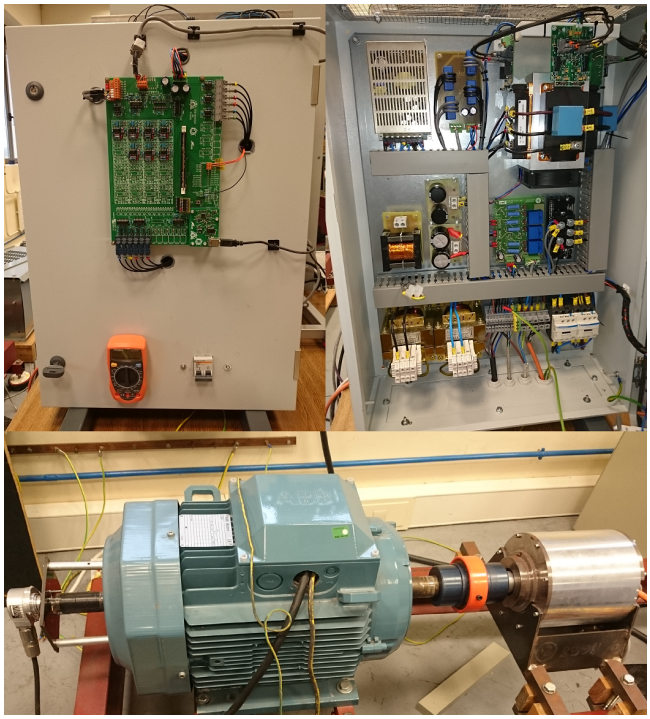

Fig. 14: Experimental setup. Top left: Control board. Top right: Power converter. Bottom: Load induction motor (left) and PMSG (right).

turbine inertia. Fig. 13(b) shows the actual turbine torque, $T_t$, and its estimate, $\hat{T}_t$. It can be seen a good matching between both magnitudes despite some ripple in the estimated torque. This is also the case when a conventional converter is used [30]. Fig. 13(c) shows the boost current command and the actual boost current. It can be seen the current control is working properly. Some ripple is seen in the actual current due to the voltage command approximation, as it was described in section IV. Fig. 13(d) shows the measured voltage after the antialiasing filter, $v_{r\_\mathrm{DSC}}$. Although it still shows a significant amount of ripple, it is confirmed that can be successfully used to both calculate the rotor speed command and the rotor speed estimate necessary to control the wind turbine. It must be remarked that the wind turbine control system has not experienced any modification or special tuning with respect to that described in [30], apart from the boost current controller, as described in section III.

Therefore, the inductorless converter can be safely used to control small wind turbines.

## VII. Experimental Results

The proposed controller for the inductorless converter for small wind turbines has been experimentally tested to validate its performance. An Alxion 190STK3M alternator whose parameters can be found in Table III is used as generator. A wind turbine with the parameters seen in Table V is emulated using a 4-pole 11 kW vector controlled induction motor drive. The turbine power curves as well as the turbine inertia are programmed in the load drive using a SM-Applications Lite module from Control Techniques. A custom converter following the design seen in Fig. 1(a) is used for the

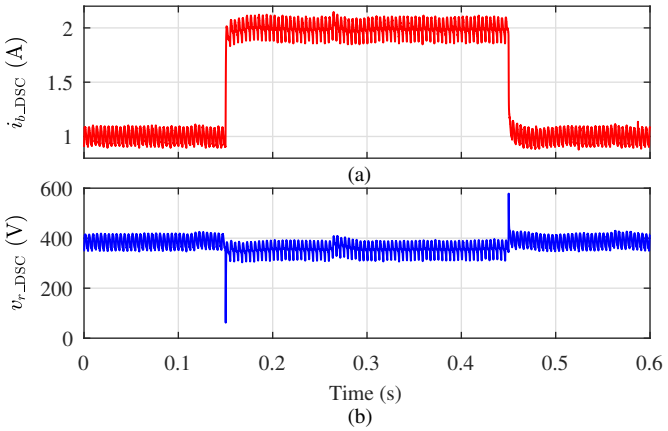


Fig. 15: Experimental result. Inductorless boost converter performance. 1 to 2 A boost current step up/down at fixed 400 r/min rotor speed. Current loop bandwidth: 400 Hz. Signals downsampled to 10 kHz. (a) Measured boost current, $i_{b\_\mathrm{DSC}}$. (b) Measured rectifier voltage $v_{r\_\mathrm{DSC}}$.

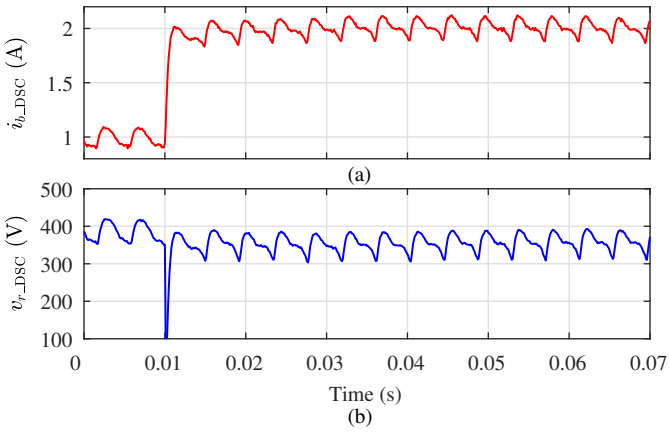


Fig. 16: Experimental result. Inductorless boost converter performance detail. 1 to 2 A boost current step at fixed 400 r/min rotor speed. Current loop bandwidth: 400 Hz. Signals downsampled to 10 kHz. (a) Measured boost current, $i_{b\_\mathrm{DSC}}$. (b) Measured rectifier voltage $v_{r\_\mathrm{DSC}}$.

generator operation. The control blocks seen in Fig. 1(b)-(c) are implemented in a Texas Instrument TMS320F28335 DSC. The PWM and sampling frequencies for the boost converter are set to 20 kHz. The H-bridge inverter switching frequency is 10 kHz. The experimental setup can be seen in Fig. 14.

The inductorless converter was first tested to confirm the boost current control capability. Fig. 15(a) shows the measured boost current when 1 to 2 A step command is imposed at $t = 0.15$s and 2 to 1 A at $t = 0.45$s. The rotor speed is controlled by the load drive to 400 r/min, and the current controller is tuned to 400 Hz, like in the simulations carried out. The measured current is perfectly controlled as predicted by the simulations. Fig. 15(b) shows the measured rectifier voltage. Despite the expected ripple, it is still a valid signal for control.

A magnified view of the current step is shown in Fig. 16. The ripple observed both in the boost current and in the measured voltage is very similar to that predicted by the simulation results. By comparison with Fig. 5(a)-(c) it can be noticed the degree of accuracy of the performed simulations. It

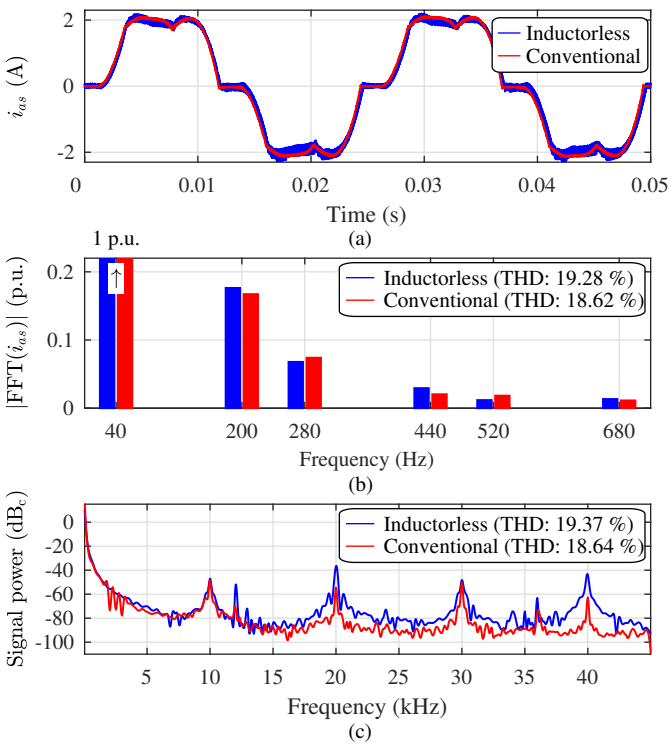


Fig. 17: Experimental result. Generator phase-a current with boost current $i_b = 2$ A, rotor speed $\omega_{rm} = 400$ r/min and DC-link voltage $v_{dc} = 575$ V, for the inductorless and conventional boost converters. (a) Phase-$a$ current. (b) Frequency spectrum of phase-$a$ current showing components higher than .01 p.u. THD calculated for harmonics up to 1 kHZ. (c) Power spectrum of phase-$a$ current. THD for harmonics up to 45 kHZ. Signals sampled at 500 kHz.

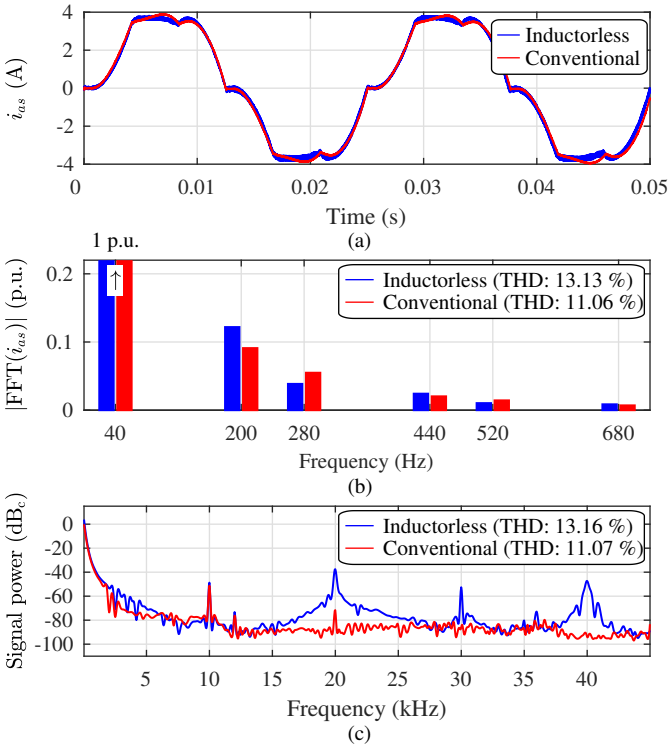


Fig. 18: Experimental result. Generator phase-a current with boost current $i_b = 3.7$ A (rated), rotor speed $\omega_{rm} = 400$ r/min and DC-link voltage $v_{dc} = 575$ V, for the inductorless and conventional boost converters. (a) Phase-$a$ current. (b) Frequency spectrum of phase-$a$ current showing components higher than .01 p.u. THD calculated for harmonics up to 1 kHZ. (c) Power spectrum of phase-$a$ current. THD for harmonics up to 45 kHZ. Signals sampled at 500 kHz.

must be remarked that no offline processing has been done to the experimental results; the measured signals being directly stored in the DSC memory for later representation.

The generator phase-a current has been acquired with a Keysight DSOX3014A digital scope for two values (2 and 3.7 A) of the boost current, as can be seen in Figs. 17 and 18. They show a close agreement with those analyzed in simulation, in Figs. 8 and 9. However, small differences exist: 1) The general harmonic content is slightly smaller than in simulation; this is easily explained by any small difference in the parameter values used in simulation from the actual values. 2) The high frequency spectrum contains harmonics at multiples of 10 kHz not seen in simulation; this is radiated noise induced in the scope probes from the H-bridge commutation. This can be clearly seen both by their low magnitude (note the logarithmic scale) and by the relative magnitude difference observed between Figs. 17(c) and 18(c), the second having an increased signal-to-noise ratio. This results confirm the analysis made by means of simulations.

The same wind sequence (11, 8, and 10 m/s) tested simulation (see Fig. 13) has been used to experimentally validate the inductorless converter for small wind turbine systems. The load drive emulates the turbine behavior including inertia using the method described in [30]. Fig. 19 shows the obtained results. It must be noticed that the variables have been down-sampled to 250 samples/s. This was due to both the test length (15 s) and the limited memory available in the DSC for data storage. Fig. 19(a) shows the rotor speed command generated to track the MPPT, $\omega^*_{rm}$, and the actual rotor speed, $\omega_{rm}$. The actual speed is obtained from the load drive encoder and it is only used for performance analysis. The actual speed accurately follows the speed command. The emulated turbine (blades) torque, $T_t$, and its estimate, $\hat{T}_t$, can be seen in Fig. 19(b). The turbine torque estimate follows the actual turbine torque within the observer bandwidth. Fig. 19(c) shows the the measured current, $i_{b\_\mathrm{DSC}}$. It can be seen the current regulation is successfully performed during the normal operation of the wind turbine. Finally, Fig. 19(c) shows the measured rectifier voltage. It can be seen the antialiasing filter provides enough attenuation to obtain a reliable signal for controlling the wind turbine.

## VIII. Conclusions

The present paper analyzes the low-cost boost converter for small wind generators where the boost coil and the input filter capacitor are removed and the boost function is made by the generator phase inductance. This can be safely made in systems using generators with a rated voltage similar to that of the DC link. This solution brings an immediate reduction of the size and cost of the system, as it has been shown. This paper demonstrates removal of the boost inductance does not require any modification in the turbine control algorithms or

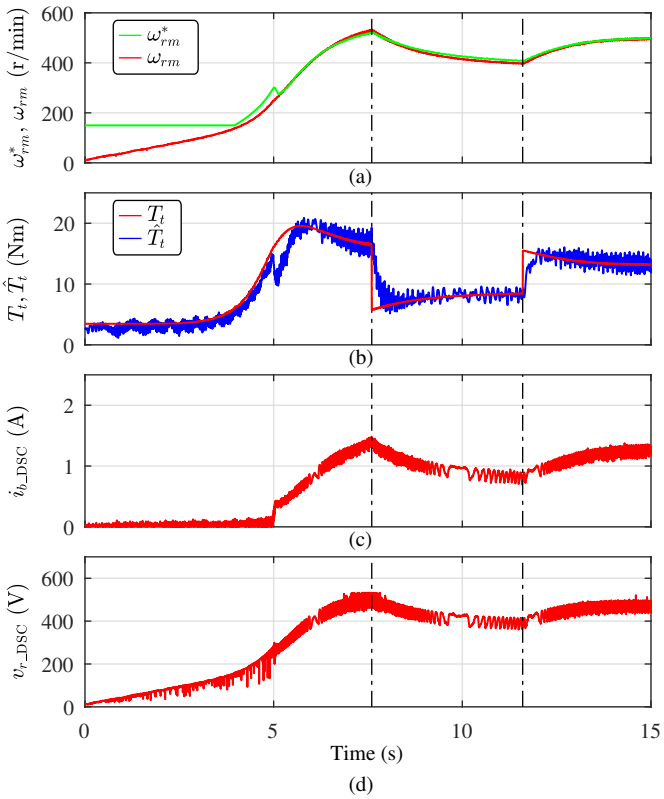


Fig. 19: Experimental result. Wind turbine control performance under variable wind conditions (11, 8, and 10 m/s indicated on top of figure). Signals downsampled to 250 Hz. (a) Rotor speed command, $\omega^*_{rm}$, and actual rotor speed, $\omega_{rm}$ . (b) Actual and estimated turbine torque, $T_t$ and $\hat{T}_t$ respectively. (c) Boost current acquired by the DSC, $i^*_b$. (d) Rectifier voltage acquired by the DSC, $v_{r\_\mathrm{DSC}}$.

the sensed variables, but a subtle change in the boost current controller, making possible system retrofitting. Moreover, the system efficiency and the generator torque dynamic response are improved. As drawbacks, a moderately higher torque ripple and slightly higher generator losses at medium to high loads have been identified. The large turbine inertia makes negligible the torque ripple increase. The higher generator losses are largely compensated by the elimination of the boost coil losses. The modification allows a better integration of the generator and the power electronics for small wind turbines. Simulations and experimental results has proven the viability of the proposed controller solution.

## REFERENCES


[1] GWEC, "Global Wind Report 2017, Annual Market Update." Global Wind Energy Council (GWEC), Tech. Rep., 2018.

[2] WWEA, "2017 Small Wind World Report Summary," World Wind Energy Association, Tech. Rep., Jul. 2017. [Online]. Available: http://www.wwindea.org/wp-content/uploads/filebase/small_wind_/SWWR2017-SUMMARY.pdf

[3] H. Li and Z. Chen, "Overview of different wind generator systems and their comparisons," *IET Renewable Power Generation*, vol. 2, no. 2, pp. 123–138, Jun. 2008.

[4] I. Schiemenz and M. Stiebler, "Control of a permanent magnet synchronous generator used in a variable speed wind energy system," in *Electric Machines and Drives Conference, 2001. IEMDC 2001. IEEE International*, 2001, pp. 872–877.

[5] M. Pathmanathan, W. L. Soong, and N. Ertugrul, "Output power capability of surface PM generators with switched-mode rectifiers," in *2010 IEEE International Conference on Sustainable Energy Technologies (ICSET)*, Dec. 2010, pp. 1–6.

[6] Y.-L. Juan, "An Integrated-Controlled AC/DC Interface for Microscale Wind Power Generation Systems," *IEEE Transactions on Power Electronics*, vol. 26, no. 5, pp. 1377–1384, May 2011.

[7] A. B. Raju, K. Chatterjee, and B. G. Fernandes, "A simple maximum power point tracker for grid connected variable speed wind energy conversion system with reduced switch count power converters," in *Power Electronics Specialist Conference, 2003. PESC '03. 2003 IEEE 34th Annual*, vol. 2, Jun. 2003, pp. 748–753 vol.2.

[8] H.-G. Park, S.-H. Jang, D.-C. Lee, and H.-G. Kim, "Low-cost converters for micro wind turbine systems using PMSG," in *7th Internatonal Conference on Power Electronics, 2007. ICPE '07*, Oct. 2007, pp. 483–487.

[9] A. Singh and B. Mirafzal, "A Generator-Converter Topology With Zero DC-Link Impedance for Direct Drive Wind Turbines," *IEEE Transactions on Energy Conversion*, vol. 32, no. 4, pp. 1620–1623, Dec. 2017.

[10] A. Singh, J. Benzaquen, and B. Mirafzal, "Current Source Generator-Converter Topology for Direct-Drive Wind Turbines," *IEEE Transactions on Industry Applications*, vol. 54, no. 2, pp. 1663–1670, Mar. 2018.

[11] S.-H. Song, S.-i. Kang, and N.-k. Hahm, "Implementation and control of grid connected AC-DC-AC power converter for variable speed wind energy conversion system," vol. 1, 2003, pp. 154–158 vol.1.

[12] H. Wang, C. Nayar, J. Su, and M. Ding, "Control and Interfacing of a Grid-Connected Small-Scale Wind Turbine Generator," *IEEE Transactions on Energy Conversion*, vol. 26, no. 2, pp. 428–434, Jun. 2011.

[13] Z. Dalala, Z. Zahid, and J.-S. Lai, "New Overall Control Strategy for Small-Scale WECS in MPPT and Stall Regions With Mode Transfer Control," *IEEE Transactions on Energy Conversion*, vol. 28, no. 4, pp. 1082–1092, Dec. 2013.

[14] C. Lumbreras, J. M. Guerrero, P. Garca, F. Briz, and D. D. Reigosa, "Control of a Small Wind Turbine in the High Wind Speed Region," *IEEE Transactions on Power Electronics*, vol. 31, no. 10, pp. 6980–6991, Oct. 2016.

[15] A. Sokolovs and L. Grigans, "Front-end converter choice considerations for PMSG-based micro-wind turbines," in *2015 56th International Scientific Conference on Power and Electrical Engineering of Riga Technical University (RTUCON)*, Oct. 2015, pp. 1–6.

[16] A. Prasad, P. Ziogas, and S. Manias, "An active power factor correction technique for three-phase diode rectifiers," in , *20th Annual IEEE Power Electronics Specialists Conference, 1989. PESC '89 Record*, Jun. 1989, pp. 58–66 vol.1.

[17] D. Simonetti, M. Azevedo, G. Sousa, and J. Vieira, "A single-switch three-phase boost rectifier with constant input harmonic content," in *Proceedings of the 24th Annual Conference of the IEEE Industrial Electronics Society, 1998. IECON '98*, vol. 2, Aug. 1998, pp. 691–696 vol.2.

[18] R. Tonkoski, L. Lopes, and F. Dos Reis, "A single-switch three-phase boost rectifier to reduce the generator losses in wind energy conversion systems," in *2009 IEEE Electrical Power Energy Conference (EPEC)*, Oct. 2009, pp. 1–8.

[19] O. Castillo, E. Amoros, G. Sanfeliu, and L. Morales, "Average Current Mode Control of Three-Phase Boost Rectifiers with Low Harmonic Distortion Applied to Small Wind Turbines," in *Electronics, Robotics and Automotive Mechanics Conference, 2009. CERMA '09.*, Sep. 2009, pp. 446–451.

[20] Y. Y. Xia, J. E. Fletcher, S. J. Finney, K. H. Ahmed, and B. W. Williams, "Torque ripple analysis and reduction for wind energy conversion systems using uncontrolled rectifier and boost converter," *IET Renewable Power Generation*, vol. 5, no. 5, pp. 377–386, Sep. 2011.

[21] D. J. Perreault and V. Caliskan, "Automotive power generation and control," *IEEE Transactions on Power Electronics*, vol. 19, no. 3, pp. 618–630, May 2004.

[22] H. Huang and L. Chang, "A new DC link voltage boost scheme of IGBT inverters for wind energy extraction," in *Electrical and Computer Engineering, 2000 Canadian Conference on*, vol. 1, 2000, pp. 540–544 vol.1.

[23] P. Tenca, A. A. Rockhill, T. A. Lipo, and P. Tricoli, "Current Source Topology for Wind Turbines With Decreased Mains Current Harmonics, Further Reducible via Functional Minimization," *IEEE Transactions on Power Electronics*, vol. 23, no. 3, pp. 1143–1155, May 2008.

[24] L. Chen, W. L. Soong, M. Pathmanathan, and N. Ertugrul, "Comparison of AC/DC converters and the principles of a new control strategy in

small-scale wind turbine systems," in *2012 22nd Australasian Universities Power Engineering Conference (AUPEC)*, Sep. 2012, pp. 1–6.

[25] D. M. Whaley, G. Ertasgin, W. L. Soong, N. Ertugrul, J. Darbyshire, H. Dehbonei, and C. V. Nayar, "Investigation of a Low-Cost Grid-Connected Inverter for Small-Scale Wind Turbines Based on a Constant-Current Source PM Generator," in *IECON 2006 - 32nd Annual Conference on IEEE Industrial Electronics*, Nov. 2006, pp. 4297–4302.

[26] R. Sharma, T. W. Rasmussen, and B. B. Jensen, "Application of a synchronous generator with a boost converter in wind turbines: an experimental overview," *IET Renewable Power Generation*, vol. 6, no. 6, pp. 414–423, Nov. 2012.

[27] M. Meiqin, L. Jidong, M. Ding, C. V. Nayar, and L. Chang, "A novel control strategy for small wind generation system based on the converter without DC storage components," in *2010 IEEE International Conference on Sustainable Energy Technologies (ICSET)*, Dec. 2010, pp. 1–5.

[28] W. Malan, D. J. Thrimawithana, and U. K. Madawala, "Performance study on a low cost converter for micro-wind generarion systems," in *IECON 2013 - 39th Annual Conference of the IEEE Industrial Electronics Society*, Nov. 2013, pp. 7193–7198.

[29] K. Buchert and F. W. Fuchs, "Power Losses of Three Phase Rectifier Topologies in Small Wind Turbines," in *Renewable Energy and Energy Management; Proceedings of PCIM Europe 2015; International Exhibition and Conference for Power Electronics, Intelligent Motion*, May 2015, pp. 1–8.

[30] J. M. Guerrero, C. Lumbreras, D. D. Reigosa, P. Garcia, and F. Briz, "Control and Emulation of Small Wind Turbines Using Torque Estimators," *IEEE Transactions on Industry Applications*, vol. 53, no. 5, pp. 4863–4876, Sep. 2017.

[31] C. Lumbreras, J. M. Guerrero, D. Reigosa, D. Fernandez, and F. Briz, "Inductorless boost rectifier for small power wind energy converters," in *2016 IEEE Energy Conversion Congress and Exposition (ECCE)*, Sep. 2016, pp. 1–6.

[32] M. Hinkkanen and J. Luomi, "Induction Motor Drives Equipped With Diode Rectifier and Small DC-Link Capacitance," *IEEE Transactions on Industrial Electronics*, vol. 55, no. 1, pp. 312–320, Jan. 2008.